POLITECNICO DI TORINO
Repository ISTITUZIONALE

A phase-field study of neck growth in electron beam powder bed fusion (EB-PBF) process of Ti6Al4V powders under different processing conditions

Original
A phase-field study of neck growth in electron beam powder bed fusion (EB-PBF) process of Ti6Al4V powders under different processing conditions / Rizza, G., Galati, M., Iuliano, L.. - In: INTERNATIONAL JOURNAL, ADVANCED MANUFACTURING TECHNOLOGY. - ISSN 0268-3768. - (2022). [10.1007/s00170-022-10204-4]

Availability:
This version is available at: 11583/2972489 since: 2022-10-21T06:56:45Z

Publisher:
Springer Science and Business Media Deutschland GmbH

Published
DOI:10.1007/s00170-022-10204-4

Terms of use:

This article is made available under terms and conditions as specified in the corresponding bibliographic description in the repository

Publisher copyright

(Article begins on next page)

28 November 2026

The International Journal of Advanced Manufacturing Technology
https://doi.org/10.1007/s00170-022-10204-4

ORIGINAL ARTICLE

A phase-field study of neck growth in electron beam powder bed fusion (EB-PBF) process of Ti6Al4V powders under different processing conditions

Giovanni Rizza[1] · **Manuela Galati**[1] · **Luca Iuliano**[1]

Received: 22 June 2022 / Accepted: 22 September 2022
© The Author(s) 2022

Abstract
Traditional sintering processes are carried out to achieve complete material densification. In an electron beam powder bed fusion (EB-PBF) process, the same sintering mechanisms occur but only with the aim to form small connections between the particles (necks). A proper neck formation is central for the EB-PBF process because, among other effects, ensures the thermal stability of the process and helps to avoid smoke phenomena. This work presents a numerical study of neck formation under the EB-PBF processing conditions. A new type of modelling is introduced for the temperature sintering load and included in a phase-field model, which simulates the neck growth during the EB-PBF process of Ti6Al4V powders. The model was validated with an ad-hoc experiment, which provided a deviation with respect to the estimated neck diameter of about 9%. The deviation was investigated by reasonably varying the processing conditions. The results showed that the thermal history, the process time scale (including also the cooling phase), and the geometrical characteristics of the particles significantly affected the sintering rate and neck radius.

Keywords Phase-field · Ti6Al4V · Electron beam melting · Oxide · Neck

1 Introduction

Sintering is an ancient technique empirically adopted to process ceramic materials and metals. Particles are bonded together by mass transport mechanisms at an atomic scale during sintering, forming solid objects [1]. Atom diffusion is activated by thermal energy and driven by a reduction of the free energy of the system [2, 3]. The main parameters that influence the sintering process are temperature, pressure, size and shape of the particles, sintering atmosphere and chemical composition of the material [2]. According to these factors, different atom diffusion mechanisms can take place. The principal mechanisms (Fig. 1) are volume diffusion from different sources (D_V), grain boundary diffusion (D_{GB}), surface diffusion (D_S), vapour diffusion (D_{Vap}) and viscous flow (η) [2, 4]. The difference between these mechanisms is the diffusion path of the atoms from the particles.

Traditional sintering processes aim to obtain high-density components with a high sintering rate. Because of that, high pressure is applied during the whole process to compact the powder particles, and a long process time is required to achieve the desired degree of density [5]. In the powder bed fusion (PBF) additive manufacturing (AM) field, the use of the term "sintering" is improper since the sintering occurs only under a thermal load and is referred to the formation of small bridges between adjacent powder particles, usually called necks [6–9]. The neck is typically non-spherical with a circular cross-section, and its profile is comparable to a one-sheet hyperboloid. In the plane containing the centres of two sintering powder particles, the neck geometry can be represented as an hyperbola that connects two circles. The geometrical features that usually are used to describe the neck geometry, and thus the sintering progression, are the neck radius and the dihedral angle. The neck radius is the minimum distance between the segment that connects the centres of the powder particles and one vertex of the hyperbola (X in Fig. 1). The dihedral angle is the angle formed between the segments that connect the vertex of the

✉ Giovanni Rizza
giovanni.rizza@polito.it

[1] Department of Management and Production Engineering (DIGEP), Integrated Additive Manufacturing Center (IAM@PoliTo), Politecnico Di Torino, Corso Duca degli Abruzzi 24, 10129 Turin, Italy

Published online: 06 October 2022

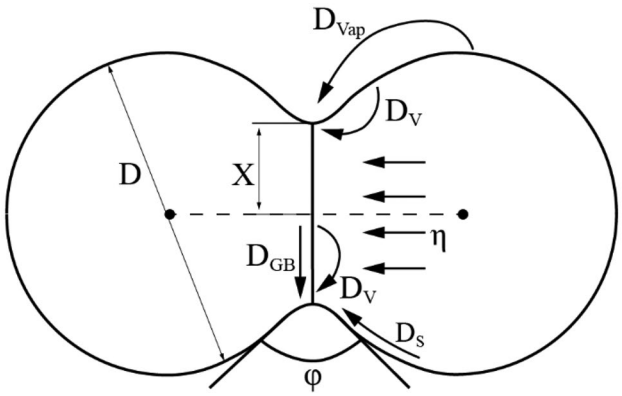


Fig. 1 Diffusion mechanisms, with respective atom sources and the main geometric dimensions. D_V is the volume diffusion, D_S is the surface diffusion, D_{GB} is the grain boundary diffusion, D_{Vap} is the vapour diffusion, and η represents the viscous flow. X represents the neck radius, D is the particle diameter, and φ is the dihedral angle

hyperbola and the point of curvature change of the profile of the sintering particles (φ in Fig. 1).

In such a process as the electron beam powder bed fusion (EB-PBF), a precise sintering degree is sought to create proper thermal and electrical stability in the powder bed during the process [10]. However, the diffusion mechanisms during an EB-PBF and other AM processes are similar to traditional sintering [11, 12].

Monte Carlo and finite element (FE) modelling are the most adopted approaches to simulate the sintering process. While the Monte Carlo method is based on a stochastic approach [13, 14], FE models consider the densification of powder particles under the effect of specific boundary conditions (temperature and pressure) [15, 16]. Because of the relatively simple modelling, both approaches fail to correlate the influence of microstructural and diffusion characteristics on the consolidation mechanisms during the sintering of three-dimensional powder particles. Additionally, those approaches cannot simultaneously account for different complex diffusion mechanisms [16, 17]. As an alternative, the phase-field modelling can consider the interaction among complex phenomena contributing to the material densification and particle movement [17, 18]. This approach is adopted in many fields such as the simulation of the diffusion [19], the solidification [20, 21], the solid-state phase transformation [22], the grain growth [23, 24], the translation of defects [25, 26], crack propagation [27–29] and other applications [16, 30, 31]. The most relevant advantage of the phase-field approach is the description of the arbitrary microstructure evolution without tracking the interface position or imposing any boundary condition [16, 17]. The microstructural characteristics, both structural/compositional and the interface, are identified as phase-field variables [16, 30]. These variables refer to specific physic parameters and assume well-defined values at the boundaries of each particle. These values can change rapidly but smoothly along with the interface of the particles [16, 32–34]. This characteristic is fundamental as the interface of particles is automatically described by the evolution of phase-field variables [16, 17, 32, 34, 35]. The field variables can be grouped into conserved and non-conserved. Conserved variables contain information about the local composition and describe characteristics such as density or molar fraction [32]. Non-conserved variables represent information about local structure and orientation. These variables may distinguish among coexisting phases with different characteristics or grains or particles [32, 33]. Changes in both conserved and non-conserved variables involve changes in the microstructure and properties of the considered system [16]. What drives the evolution in space and time of the variables is the reduction of the system free energy [16, 36], which is built as a functional of the conserved and non-conserved variables.

Cordero et al. [46] developed a comprehensive phase-field model that investigated the effect of beam parameters on melt pool geometry, porosity and microstructure. Zhang and Liao [37] and Yang et al. [38] proposed a phase-field model to predict microstructure evolution after the melting phase of the laser powder bed fusion (L-PBF) process. In these cases, phase field models are adopted to simulate the melting, the following solidification and the final microstructure. The sintering was only evaluated as a side effect to consider the particles close to the melt pool. Similarly, Wang et al. [39] used a multi-scale phase-field model to analyse the sintering effect among the particles when the beam power during an L-PBF process is insufficient for complete melting. Gong and Chou [40] and Sahoo and Chou [41] proposed phase-field models to evaluate dendritic growth during the EB-PBF process. The effect of temperature gradients and solidification velocities [40] and the effect of undercooling [41] have been considered. Yan et al. [42] investigated the sintering during a single electron beam passage, corresponding to a millisecond time scale. They found that solid-state sintering is the driving mechanism for the sintering. The environment temperature, material properties, and particle size were identified as the most affecting parameters for the sintering. On the contrary, the processing parameters and the grain structure were found insignificant because of the small time scale investigated. All the simulations were run considering an EB-PBF performed at a constant temperature, while the temperature variation at different time scales was not investigated. In the EB-PBF, the temperature evolution over the powder bed changes significantly between milliseconds for a single beam passage to seconds for processing a single layer or hours or days for completing the component manufacturing. For example, the powder particles previously contained in the hoppers, after the spreading, increase their

temperature because of conduction and irradiation phenomena from the substrate. The next phase, preheating, which precedes the melting phase, is designed to achieve gradually an even higher temperature, up to 60–70% of the melting point of the processed material [43–45]. Then, thanks to the vacuum environment, the additional heat provided during the subsequent layers preserves a high working temperature over the entire build. Therefore, it is presumable that the formation and growth of the necks between the powder particles during the EB-PBF is a phenomenon that may be influenced by the non-isothermal conditions and wide range of time scales typical of the EB-PBF process.

This work introduces a new modelling approach to describe the processing temperature conditions that may influence the sintering during an EB-PBF process. The new formulation is implemented in a phase-field model to simulate the neck growth during the EB-PBF process of Ti6Al4V powders. The paper is organized as follows. Firstly, an overview of the sintering during the EB-PBF process explains the reasons for performing sintering during EB-PBF, the adopted strategies and the factors that may influence the sintering degree. Next, the new modelling for the temperature evolution is presented and integrated into a phase-field model. The validation section compares numerical and experimental results using an ad-hoc designed test. Then the sintering process is investigated, emulating the effect of different factors on the sintering degree. In particular, the presence of sintering delay due to, e.g. the presence of an oxide layer on the particles surface, the sintering in a group of particles and different process time scales (seconds corresponding to the preheating phase and hours for considering an example of an entire EB-PBF job) have been investigated.

2 Sintering during EB-PBF

The partial sintering of the powder during an EB-PBF process is extremely important for several reasons. The most known and critical is preventing the pushing phenomenon, known as "smoke" [8, 46]. In the case of smoke, the process is nearly unfeasible because the powder particles are removed from the powder bed and diffused in the build chamber, creating an uneven powder layer. Additionally, in the case of violent smoke phenomena, the particles could be pushed up to the electron gun, damaging the EB-PBF system. Although the causes behind the smoke are still not well known, in literature, this phenomenon is usually associated with the accumulation of negative electrostatic charges in the powder bed due to the beam passages [10, 47] or the momentum transferred by the electrons if larger than the weight of powder particles [48].

The sintering by preheating has been the first published solution to prevent smoke by increasing the apparent weight of the particles of the powder bed and its electric conductivity through the necks, allowing a better dispersion of negative charges [10]. Moreover, the formation of necks during the sintering has other beneficial effects due to the enhanced powder bed thermal conductivity [9, 49, 50]. The presence of necks helps to keep a uniform and stable temperature over the layer. Along the build volume, they decrease the thermal gradients between the melt pool and the surrounding and increase the dissipation of heat generated during the melting of overhang structures [49, 51]. Additionally, the sintered particles have a certain strength which allows a reduction of support structures [51], enhancing the possibility of producing micro-architectured and metamaterials [6, 52] and facilitating the nesting of components for exploiting the full build envelope.

Owing to the similarity with the traditional sintering process, chief among the factors that influence the sintering degrees and, therefore, the neck growth is the working temperature at which the EB-PBF is carried out. As mentioned above, this temperature is strongly influenced by the preheating step. Each EB-PBF supplier adopts a different preheating strategy. For Arcam machines, the preheating phase consists of a series of passages of a defocused electron beam that scans the powder bed at a high current (about 30 mA) and speed (about15000 mm/s) [53] in two steps: preheating one and preheating two. During preheating one, the preheated area corresponds to the maximum rectangular area, including all the areas to be melted. During preheating two, the heated area is smaller and corresponds to an offset of the section to be melted [10, 53, 54]. The following main process parameters define the sintering degree: the beam speed, the beam current, the number of scan repetitions and the distance between adjacent scanned lines [10, 55]. The proper combination of these parameters also defines powder bed temperature. A helium flow is also used to disperse better the electrical charges accumulated during the interaction between the beam and the powder particles. Recently, Freemelt One filed a patent application for a preheating procedure named ProHeat® [56]. In this case, the electron beam is used to warm up a heat-resistant metal plate, such as tungsten or graphite, and placed at 1–2 mm from the powder bed. The heated metal plate emits energy as photons in the infrared wavelength region, capable of heating locally the powder bed and producing the required sintering level. Since the electron beam does not interact with the cold powder bed, no negative charge is accumulated in the particles. Therefore, this preheating strategy allows running the EB-PBF process without the risk of smoke and without using helium. The company JEOL proposed an alternative approach to neutralize the negative charge of the powder bed [57]. The machine is equipped with two different electron beams. The primary beam is adopted to melt the powder particles, while a secondary electron beam, tilted 45 degrees

with respect to the build platform, is adopted to irradiate the entire powder bed, perform the sintering and prevent the electrostatic charge of the powder particles without the usage of inert gas. Thanks to the vacuum environment and the preheating step, the typical working temperature during an EB-PBF is high, and it ranges, e.g. between 700 °C [58, 59] and 1050 °C [59–62] for titanium alloys.

Besides the scanning strategy, the sintering degree is also affected by the size of powder particles and surface oxide present on the powder particles [2, 63]. EB-PBF generally uses spherical particles with a diameter, in a virgin state, ranging between 45 and 105 µm [64, 65]. Although the entire process is conducted under a vacuum [53], powder oxidation may occur on the surface of powder particles during handling, sieving and blasting [66]. The presence of oxide on the particle change locally the diffusion coefficients and the influence on the sintering degree depends on the considered alloy [67]. In the case of titanium, the oxide layer is dissolved as atomic oxygen in the metal matrix under high temperatures [68, 69], causing only a delay on the sintering initiation. The maximum thickness of metal oxide that can be dissolved depends on the particle dimension. The delay in the sintering initiation therefore is the time necessary to dissolve the oxide layer, called incubation time. During this time, the neck formation is inhibited [68, 69]. Munir [68, 69] analytically evaluated an incubation time of 5.87×10^{-3} s at temperatures higher than 1273 K for titanium particles (with a diameter of 9.71 µm) coated with an oxide layer of 10 nm. These analytical results contrast with the experimental results obtained by Watanabe and Hirokoshi [70], which identified a more considerable incubation time equal to around one hour. Munir [68, 69] stated that the difference between analytical and experimental times could be related to the titanium matrix oxygen saturation, which hinders oxygen diffusion. On bigger particles, Cao et al. [71] identified a surface oxide thickness on EB-PBF Ti6Al4V powders that ranges from 6.5 nm for the virgin powders to 7.54 nm for powder after ten recycles. The oxide layer was always thinner than that one presented in Munir [69] and Wanatabe and Horikoshi [70]. To the best of the author's knowledge, no literature is currently available about the incubation time for Ti6Al4V powder particles processed with AM processes. However, it is reasonable to presume that the incubation time is shorter with a thinner oxide layer and for lower values of the ratio between the oxide and particle diameter [68, 69].

3 Modelling of the processing temperature profile during the EB-PBF process

The thermal history during an EB-PBF process can be described by the different contributions which can be resumed, in sequential time order, as follows: (1) heat transfer between the material substrate and the deposited layer that takes place after the powder spreading and during the levelling phase; (2) heat transfer due to the beam passages during the preheating phase; (3) heat transfer between the melted material and the surrounding during the melting phase; (4) heat transfer during an eventual post-heating or cooling [59]; (5) heat transfer due to the deposition and the melting of subsequent layers; (6) heat transfer at a steady-state condition corresponding to the working temperature of EB-PBF up to the build conclusion; (7) heat transfer after the build end, during the cooling under a controlled environment up to the safe temperature to remove the job from the machine.

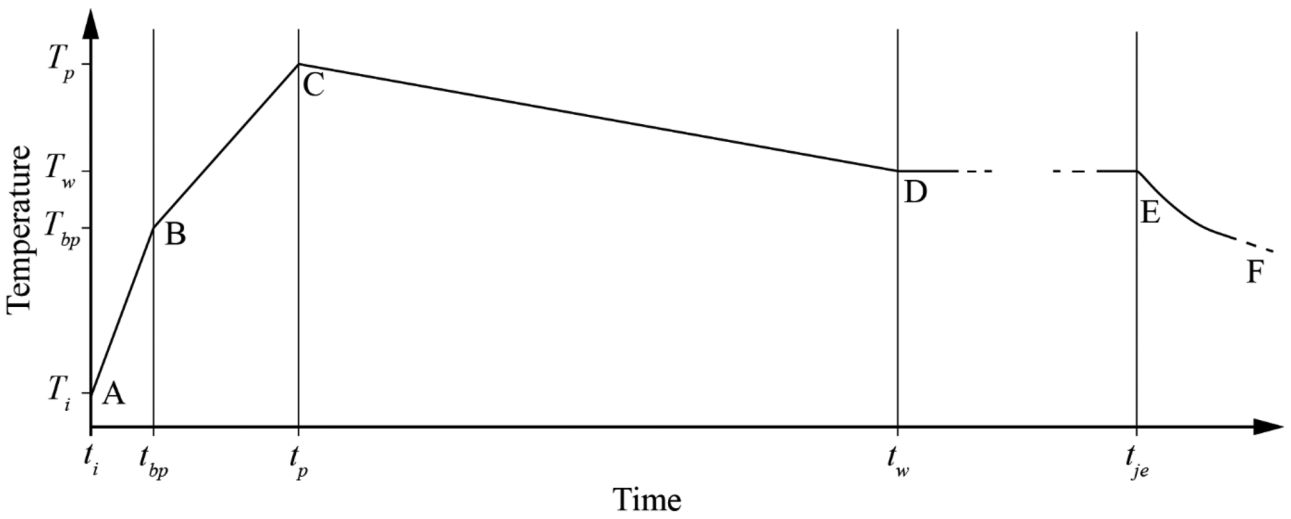


Fig. 2 Representation of the temperature evolution for powder particles raked on the building area: raking (AB), preheating (BC), inter-layer cooling (CD), steady-state condition at working temperature (DE) and final job cooling under helium (EF)

This thermal history can be modelled as in Fig. 2, in which, for simplicity, contributions (3) and (4) were not considered.

The heat transfer of the powder begins when the powder is distributed on the previous layer (segment AB). The heat transfer mainly occurs for thermal conduction between the substrate and the actual powder bed layer. Therefore, this phase is modelled as a linear increase of the temperature from the initial value of the powder bed after the spreading (T_i) up to the powder bed temperature before the preheating phase (T_{bp}). The time during which the heat transfer takes place is the time required for levelling the powder bed after the powder spreading (t_{bp}). Practically, T_{bp} can be estimated by simulating the heat transfer during the levelling phase and considering a temperature of the substrate equal to the working temperature (T_w), t_{bp} and the actual powder thermal conductivity. T_{bp} was forecasted in this work using a thermal finite element (FE) simulation. During the preheating phase (BC in Fig. 2), the powder bed temperature is increased gradually according to the sintering strategy described in the previous paragraph. The model of the thermal load for the sintering considered a stepped increase from T_{bp} to the predefined preheating temperature (T_p). This stepped increase of temperature emulates, e.g. the subsequent beam passages. The contribution (5) (segment CD in Fig. 2) emulates the heat transfer occurring during the deposition of the following layers on powders sufficiently far from the melting area. At this stage, the observed layer can be considered in the critical substrate thickness, beyond which its temperature will not be significantly affected by the heating provided by the beam during the process [72]. During this step, the main effect is associated only with the conductive heat transfer without any energy provided by the upper layers. The segment CD is modelled as a linear decrease of temperature up T_w. The associated time required to reach the working temperature, t_w, depends on the processing conditions. However, in this stage, the temperature drop is considered rapid in a time corresponding to the time to process one layer, according to Shen and Chou [72]. Segment DE in Fig. 2 represents a steady-state condition in which the sintering is only influenced by the actual T_w [45] until the build job end (t_{je}). The contribution (7) (EF in Fig. 2) represents the cooling phase. This phase starts when the last layer is completed, and the build chamber is filled with helium to facilitate the cooling. Therefore, the cooling is due to a combined effect of conduction and convection heat transfer and modelled as a parabolic descendant profile, with a progressive reduction of the temperature up to the safe temperature. The parabolic function will depend on the building height, the quantity of bulk material with respect to the sintered powder, and the degree of sintering of the powder surrounding the manufactured parts. The temperature profile can be expressed as a function of time as defined in Eq. (1).

$$T(t) = \begin{cases} T_{bp} + int\left(\frac{t-t_{bp}}{t_p-t_{bp}}n\right)\frac{T_p-T_{bp}}{n} & \forall t_{bp} \le t \le t_p \\ T_p + \frac{T_w-T_p}{t_w-t_p}(t-t_p) & \forall t_p < t \le t_w \\ T_w & \forall t_w < t \le t_{je} \\ a(t-t_{je})^2 + b(t-t_{je}) + c & \forall t > t_{je} \end{cases} \quad (1)$$

where n is the number of temperature steps of the selected stepped function (segment BC) and a, b and c are the coefficients of the cooling parabolic profile.

4 Phase-field model

The reduction of the free energy of the system is the principle that guides its evolution in the phase-field method. Equation (2) reports the formulation of the system free energy adopted in the current work. This formulation of free energy was proposed by Biswas et al. [36]:

$$F = \int \left[f(c,\eta_i) + \frac{1}{2}k_c|\nabla c|^2 + \frac{1}{2}\sum\nolimits_i k_{\eta_i}|\nabla \eta_i|^2 \right] dV \quad (2)$$

Equation (2) consists mainly of three terms. The first term $f(c,\eta_i)$ represents the bulk free energy. The second represents the excess of energy at the interface solid/void. The third represents the excess energy at the particle boundary interface [36]. System free energy is a function of conserved and non-conserved field variables represented by the terms c and η_i, respectively. For the current work, the conserved field represents the matter concentration, assuming a value of 1 inside the material and 0 outside. The non-conserved field represents the morphology of the system, and η_i assumes a value of 1 inside the i-th particle and 0 outside. This variable allows a distinction between the particles of the system. The interface of powder particles is characterized by a rapid but smooth transition of the field variables from 1 to 0, moving from the inside to the outside of the particles.

The first term of Eq. (2) is the bulk free energy, which is reported in Eq. (3).

$$f(c,\eta_i) = Ac^2(1-c)^2 + B\left[c^2 + 6(1-c)\sum\nolimits_i \eta_i^2 - 4(2-c)\sum\nolimits_i \eta_i^3 + 3\left(\sum\nolimits_i \eta_i^2\right)^2\right] \quad (3)$$

In Eq. (3), A and B are two coefficients related to material properties, described by Eqs. (4) and (5).

$$A = \frac{(12\gamma_s - 7\gamma_{GB_{ij}})}{\delta} \tag{4}$$

$$B = \frac{\gamma_{GB_{ij}}}{\delta} \tag{5}$$

where γ_s and γ_{GBij} represent the surface and grain boundary energy, respectively, and are material dependent. δ represents the interface width, i.e. the distance along which occurs the transition of the field variables. The gradient coefficients of the second and third terms of Eq. (2) are explicated in Eq. (6) and (7)

$$k_c = \frac{3}{4}\delta\left(2\gamma_s - \gamma_{GB_{ij}}\right) \tag{6}$$

$$k_{\eta_i} = \frac{3}{4}\left(\delta\gamma_{GB_{ij}}\right) \tag{7}$$

The time and space evolution of conserved variable c is described by the Cahn–Hilliard (CH) equation, reported in Eq. (8) which represents a diffusion equation [32, 73].

$$\frac{\partial c(\boldsymbol{x},t)}{\partial t} = \nabla\cdot\left(\boldsymbol{M}\cdot\nabla\frac{\delta F}{\delta c(\boldsymbol{x},t)}\right) = \nabla\cdot\left[\boldsymbol{M}\cdot\nabla\left(\frac{\partial f}{\partial c} - k_c\nabla^2 c\right)\right] \tag{8}$$

The term $\boldsymbol{M}$ represents the concentration mobility tensor, and the terms $\boldsymbol{x}$ and t represent the spatial position vector and simulation time. The concentration mobility tensor is described by Eq. (9).

$$\boldsymbol{M} = \frac{\boldsymbol{D}\Omega}{k_b T} \tag{9}$$

where $\boldsymbol{D}$ is the diffusivity tensor, Ω is the molar volume of the material considered, k_b is the Boltzmann constant, and T the temperature of the system, which was implemented according to Eq. (1). The diffusivity tensor $\boldsymbol{D}$ is the sum of the contributions of volume, surface and grain boundary diffusion and is described by Eq. (10) [36, 73]. The diffusivity tensors are calculated using Eqs. (11), (12) and (13).

$$\boldsymbol{D} = \boldsymbol{D}_V + \boldsymbol{D}_S + \boldsymbol{D}_{GB} \tag{10}$$

$$\boldsymbol{D}_V = D_V\phi_b(c)\boldsymbol{I} \tag{11}$$

$$\boldsymbol{D}_S = D_S\phi_s(c)\boldsymbol{T}_s \tag{12}$$

$$\boldsymbol{D}_{GB} = D_{GB}\sum_i\sum_j \eta_i\eta_j\boldsymbol{T}_{GB_{ij}} \tag{13}$$

where D_V, D_S and D_{GB} represent the volume, surface, and grain boundary diffusion coefficients, respectively, $\phi_b(c)$ and $\phi_s(c)$ are the interpolation functions and $\boldsymbol{I}$, $\boldsymbol{T}_s$ and $\boldsymbol{T}_{GBij}$ represent the identity matrix and the projection tensor of surface and grain boundary diffusion, respectively. An Arrhenius-type equation was used to describe the volume, surface and grain boundary diffusion coefficients. An example of this equation is reported in Eq. (14), where D^0 represents the pre-exponential factor that characterizes each diffusion term, Q is the activation energy relative to that specific diffusion mechanism, k_b is the Boltzmann constant, and T represents the temperature of the system, which was implemented according to Eq. (1).

$$D = D^0 exp\left(-\frac{Q}{k_B T}\right) \tag{14}$$

Equations (15) and (16) describe the interpolation functions as a function of the concentration field c.

$$\phi_b(c) = c^3\left(10 - 15c + 6c^2\right) \tag{15}$$

$$\phi_s(c) = 30c^2(1-c)^2 \tag{16}$$

The projection tensors are reported in Eqs. (17) and (18), where $\boldsymbol{n}_s = \nabla c/|\nabla c|$ is the unit vector normal to the interface particle void and $\boldsymbol{n}_s = (\nabla\eta_i - \nabla\eta_j)/|\nabla\eta_i - \nabla\eta_j|$ is the unit vector normal to the grain boundary surface.

$$\boldsymbol{T}_s = \boldsymbol{I} - \boldsymbol{n}_s \otimes \boldsymbol{n}_s \tag{17}$$

$$\boldsymbol{T}_{GB_{ij}} = \boldsymbol{I} - \boldsymbol{n}_{GB_{ij}} \otimes \boldsymbol{n}_{GB_{ij}} \tag{18}$$

Equation (19) represents the Allen–Cahn (AC) equation [32, 73], which describes the evolution of non-conserved variables.

$$\frac{\partial\eta_i(\boldsymbol{x},t)}{\partial t} = -L\left(\frac{\delta F}{\delta\eta_i(\boldsymbol{x},t)}\right) = -L\left(\frac{\delta f\left(c,\eta_i\right)}{\delta\eta_i} - k_{\eta_i}\nabla^2\eta_i\right) \tag{19}$$

The term L represents the order parameter scalar mobility and is explicated in Eq. (20). ϑ_{GB} is the grain boundary mobility and is expressed by an Arrhenius type equation (Eq. (14)), in which the temperature dependency was implemented according to Eq. (1).

$$L = \frac{\vartheta_{GB}\gamma_{GB}}{\kappa_{\eta_i}} \tag{20}$$

Equations (2), (8) and (19) were implemented in Multiphysics Object-Oriented Simulation Environment (MOOSE) [74], an open-source parallel finite element framework developed at Idaho National Lab. Equation (8) is a fourth-order differential equation and was implemented with two second-order differential equations as reported in Eqs. (21) and (22).

$$\frac{\partial c}{\partial t} = \frac{\partial}{\partial x_i}\left(M_{ij}\frac{\partial\mu}{\partial x_j}\right) \tag{21}$$

$$\mu = \frac{\partial f}{\partial c} - \kappa_c \nabla^2 c \tag{22}$$

In MOOSE, the differential Eqs. (21), (22) and (19) were implemented in the week form as reported in Eqs. (23), (24) and (25).

$$\left(\frac{\partial c}{\partial t}, \psi_m\right) = \left(M\nabla\mu, \nabla\psi_m\right) - \langle M\nabla\mu.\vec{n}, \psi_m\rangle \tag{23}$$

$$\left(\mu, \psi_m\right) = \left(\frac{\partial f}{\partial c}, \psi_m\right) + \left(k_c\nabla c, \nabla\psi_m\right) - \langle k_c\nabla c.\vec{n}, \psi_m\rangle \tag{24}$$

$$\left(\frac{\partial \eta_i}{\partial t}, \psi_m\right) = -L\left(\frac{\partial f}{\partial c}, \psi_m\right) + L\left(k_{\eta_i}\nabla\eta_i, \nabla\psi_m\right) - L\left(k_{\eta_i}\nabla\eta_i.\vec{n}, \psi_m\right) \tag{25}$$

where ψ_m represents the test function, $(\cdot)$ represents a volume integration and $\langle\cdot\rangle$ represents a boundary integration. The concentration mobility tensor links Eqs. (23), (24) and (25) with the temperature of the system, which was implemented according to Eq. (1).

As above mentioned, the model was implemented in MOOSE [74] and considering a two-dimensional rectangular domain of calculation. The dimensions of the simulated domain were fixed to contain the powder particles totally and an additional portion of domain that simulates the presence of vacuum environment. The space between the particles contour and the perimeter of the domain has been fixed equal at least to 5 µm. This value has been adopted to keep low the ratio between the empty and solid material and to avoid effect of domain boundary on the material diffusion [75]. The simulations were initialized by specifying the initial condition for conserved and non-conserved variables. The initial values specified allowed to distinguish numerically the solid material of the powder particles and the surrounding vacuum environment. The temperature of the system was specified for the overall domain. Additional details about the implementation of the model are provided in next sections according to the investigated aspects.

5 Model validation

The phase-field model proposed has been validated against an ad-hoc designed experimental run. With this scope, an Arcam A2X and Ti6Al4V powder were adopted.

Because of the difficulty of measuring the actual temperature of the powder bed, the experiment was designed to use the information provided by the thermocouple positioned below the start plate. However, this only gives somewhat precise information about the working temperature at the beginning of the process. Along with the process, these measurements were affected by the thermal conductivity of the deposited layers and melted zones. Therefore, this data is no longer representative of the actual powder bed layer temperature. To overcome the difficulties in measuring the temperature of the powder bed, only a few layers of powder have been processed. The total thermal energy supplied by the electron beam during the preheating has been calibrated to have only the amount of energy necessary to maintain a constant temperature of the platform.

The experiment consisted of the sintering of thin layers of powder deposited on a thick preheated start plate, in which the temperature was monitored using a thermocouple positioned below it. The stainless steel start plate had the dimension of 210 mm × 210 mm and was positioned on top of a powder substrate 70 mm thick to ensure thermal insulation from the build tank. The start plate was heated for 30 min up to approximately 1131 K. Then, the start plate was lowered of 0.050 mm, and a layer of powder was spread and uniformly heated using the parameters reported in Table 1. These steps were repeated three times for a total build height equal to 0.150 mm. After that, the process was stopped, and the chamber was filled with helium to reproduce the cooling phase in a real job and cooled down up to 353 K. Figure 3 shows a schematic representation of the experimental setup adopted for the validation. The thermocouple is positioned in contact with the bottom surface of the start plate, that is positioned on top of a powder layer contained in the build tank. The powder is fed by gravity from the left and right hoppers and distributed by the rake system that collects a certain quantity of powder from left and right, alternatively. The hoppers are located in the upper part of the build tank [76].

Figure 4 reports the temperature evolution as measured by the thermocouple below the start plate during the whole experiment. Phase 1 represents the start plate heating up to 1131 K for a time equal to 1800s (30 min). Phase 2 represents the phase where the layers of powder have been processed. The total required time was 60 s. During this time, as shown in the magnification in Fig. 4, the temperature remained constant and equal to 1131 K, meaning that the start plate acts as a heat accumulator and the thermal energy provided by the electron beam during the preheating of the layer only served to maintain constant the

Table 1 The preheating parameters adopted for processing Ti6Al4V alloy in Arcam A2X machine

Parameter	Preheating 1	Preheating 2
Beam current [mA]	30	38
Beam speed [mm/s]	10000	13000
Number of repetitions	2	3
Line offset [mm]	1.2	1.2
Focus offset	70	70

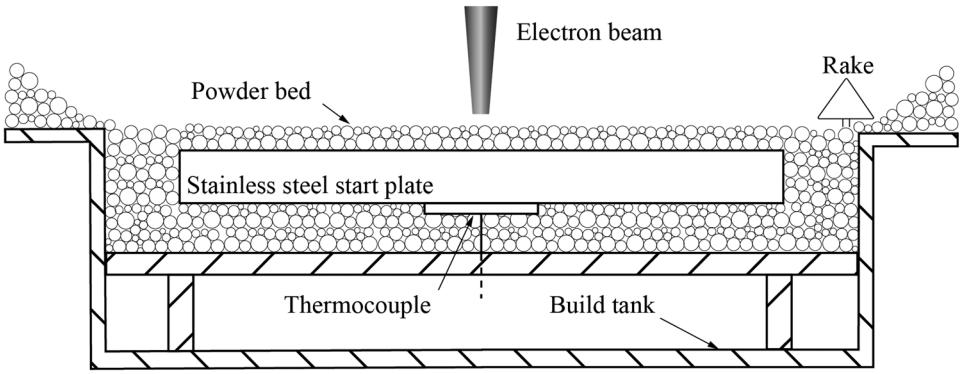


Fig. 3 Schematic representation of the EB-PBF build chamber. This figure is not to scale

temperature. Phase 3 is the cooling phase which required approximately 6180 s. As mentioned above, the temperature trend is approximately parabolic due to the combined effect between the conduction and the convection. The total time was 8040 s.

Figure 5a reports a picture of the start plate extracted from the chamber. Necks between adjacent particles can be observed all over the layers, as shown in the magnification in Fig. 5b. Two couples of two powder particles with similar diameters (couple A and B, highlighted in Fig. 5b) were selected to validate the model. Couple A is constituted of two powder particles with a diameter of 58.03 ± 3.65 µm and 69.76 ± 3.42 µm. Couple B is constituted of two particles with a diameter of 62.59 ± 3.67 µm and 65.48 ± 3.80 µm. The corresponding measured neck diameters were equal to 18.12 ± 6.87 µm and 18.91 ± 2.30 µm, for the couple A and B, respectively. The reported deviation is obtained as the average of five measurements and is due to the non-perfect spherical shape of the particles and the accuracy of the optical microscope (Leica DM2700 M).

The experimental setup was replicated in the simulation environment, and the sintering of two couples of Ti6Al4V powder particles was simulated. Table 2 resumes the geometrical information of the numerical model.

The initial mesh dimension was set at 1 µm, and an adapting refinement algorithm was adopted to refine the mesh at the particle interface. The 2D elements adopted for the simulation were triangular with six nodes (TRI6). The initial interface width was equal to 2 µm, corresponding to two elements. However, from the first simulation step, the mesh refinement at the interface ensures the presence of at least four elements, in agreement with Ivannikov et al. [77]. The initial time step was set equal to 10^{-3} s. During the simulation, the time step was increased to speed up the simulation, fixing a maximum value equal to 10 s for stability reasons. The simulation emulates the sintering conditions of the powder bed after the powder spreading.

The thermal load has been modelled according to Eq. (1). As mentioned above, the temperature of the powder particles at the end of the raking phase and before the preheating, T_{bp}, was obtained using the thermal FE model developed and validated by Galati et al. [59, 78, 79]. The model was used to simulate the steady heat transfer between a solid substrate and a powder bed with certain initial temperatures for

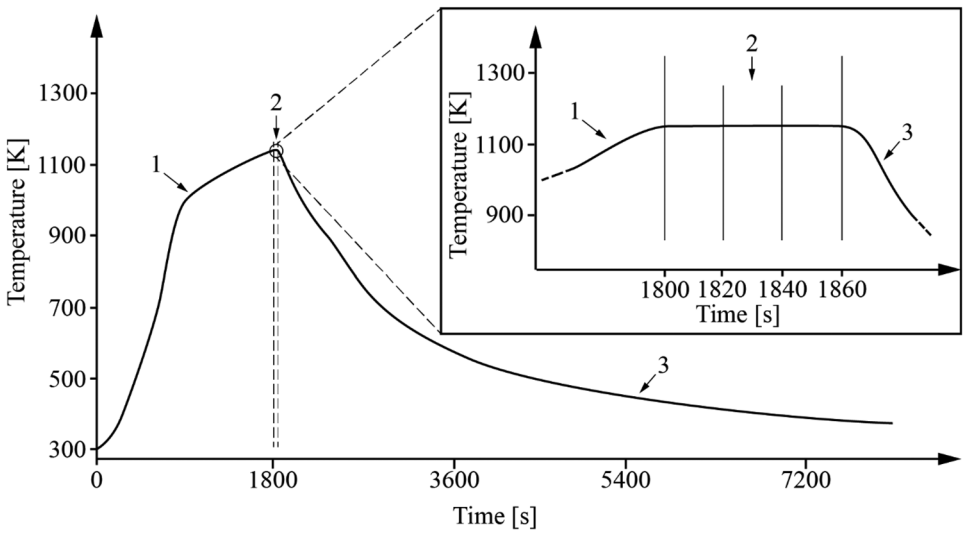


Fig. 4 Temperature profile generated from the measurements of the thermocouple positioned below the start plate. (1) Start plate preheating; (2) Job processing; (3) Cooling inside the build chamber

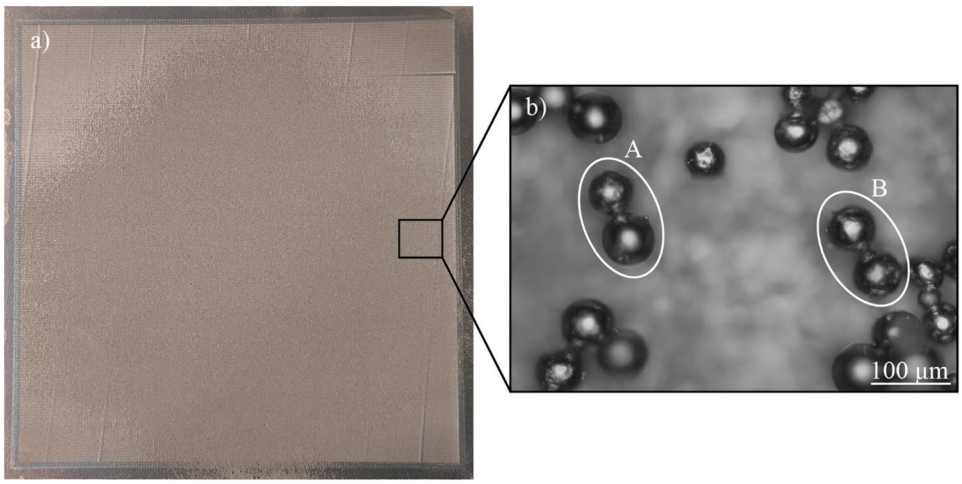


Fig. 5 **a** Start plate with sintered powder and **b** optical image of the powder particles partially sintered. The light grey background in the optical microscopy image is the start plate. Highlighted with white ellipsoid are the two couple of powder particles adopted as a reference for the model validation

a certain time corresponding to t_{bp}. The FE model consisted of a powder layer with a thickness of 0.050 mm modelled on the top of a solid stainless steel substrate 10 mm thick. The model was implemented in Abaqus 2017. The domain was discretised using 8-node linear heat transfer bricks (D3C8) with a size of 0.050 m, which is comparable with the particles size. The material properties for the powder were extracted from Galati et al. [78]. The initial temperature of the substrate and the powder layer was set equal to 1131 K and 353 K, respectively. The simulation time (t_{bp}) was set equal to 4.4 s, corresponding to the levelling time according to the standard procedure of an Arcam A2X, which corresponds to three subsequent rake passages [80].

For completeness, as an example, Fig. 6 reports a portion of a typical log file data regarding the rake current and the beam current, in which the complete process, including the melting, has been performed. In Fig. 6, the first peak on the rake current profile represents the powder fetch, the second peak represents the spreading movement, and the following two peaks represent the levelling movements. The total rake time (t_{bp}) is highlighted in Fig. 6. After the levelling phase, the rake rests out of the building volume. The oscillations of the rake current during the resting time can be considered noise. When the rake is moving, the beam current value equals zero. During preheating 1 and 2, the beam current has a constant value [7]. During the melting, the beam current is adapted according to the length of the line to be scanned [7]. During the post-heating, the beam current is constant and equal to the one used for the preheating 2. While preheating 1 and 2 have a fixed duration equal to t_p, the melting and the post-heating/cooling duration change according to the melted section [7].

Table 2 Geometrical data for the simulation model setup

	Diameter 1 [µm]	Diameter 2 [µm]	Domain size [µm^2]
Couple A	58.03	69.76	80×135
Couple B	62.59	65.48	75×135

Figure 7 shows the temperature evolution of a node in the centre of the powder layer as resulting from the FE analysis. The powder bed temperature increases due to the heat transfer from the substrate, reaching 982 K. This temperature has been set as T_{bp} value in Eq. (1).

Because no temperature variation has been observed during the preheating of the powder layers (magnification in Fig. 4), T_p and T_w were assumed equal to the start plate temperature (1131 K). The simulation time was set equal to 60 s, corresponding to the time to process the three powder layers (60 s). Because the job was stopped at the end of the third layer, the stage corresponding to the segment DE (Fig. 2) is absent. The cooling phase was modelled using a regression model (confidence interval 95%, R^2 95.93%) on the temperature profile recorded by the thermocouple. The total simulation time was 6240 s. Equation (26) resumes the temperature profile implemented in the model.

$$T(t) = \begin{cases} 982 + 15.68t & \forall 0 \le t \le 9.5 \\ 1131 & \forall 9.5 < t \le 60 \\ 2.75 \cdot 10^{-5}(t-60)^2 - 0.27(t-60) + 1131 & \forall t > 60 \end{cases} \quad (26)$$

The material properties adopted for the simulations are reported in Table 3. Grain boundary diffusion was considered equal to a tenth of the surface diffusion, while vapour diffusion and viscous flow were neglected. The material properties were converted in non-dimensional quantities adopting a length scale coefficient equal to $1 \cdot 10^{-6}$ m, a time scale coefficient of 1 s and an energy coefficient equal to $1 \cdot 10^{9}$ eV. Non-dimensional parameters were automatically evaluated using the implemented functions.

Figure 8 and Table 4 compare experimental and numerical results. Overall, the comparison showed a good agreement between the numerical and experimental

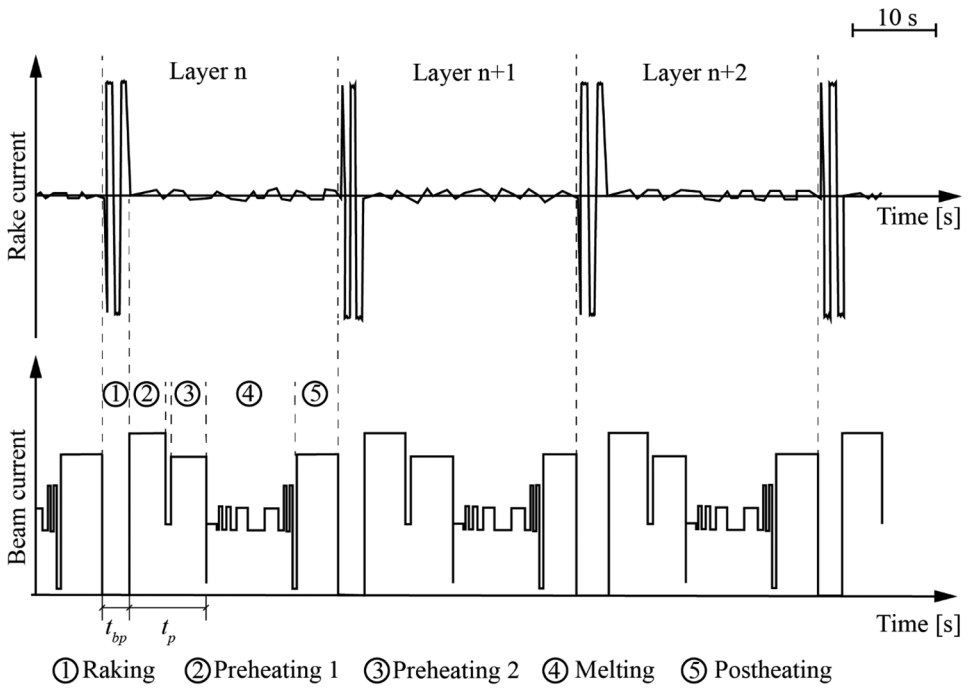


Fig. 6 Rake current and beam current profile during an EB-PBF process extracted from an Arcam A2X. Each peak of the rake current represents a movement of the rake. The first peak on the rake current represents the powder fetch, the second peak represents the spreading movement, and the following two peaks represent the levelling movements. t_{bp} is the total rake time. When the rake is moving, the beam current is equal to zero

measurements. In both cases, A and B, the necks obtained from numerical simulation have a dihedral angle larger than the experimental counterpart (Fig. 8b, d). The neck geometry obtained from numerical is more regular than that obtained experimentally, with a smooth transition from the particle surface to the neck surface. The estimated numerical neck diameter is always greater than the experimental counterpart. The most significant deviation, below 10% (Table 4), was observed for couple A in which the measured diameters and neck were affected most by the measuring system. This deviation may be attributed to phenomena that have been neglected or challenging to consider from the experimental and numerical points of view. For example, the smaller neck diameter in the case of experimental measurements may be attributed to sintering delays due to, e.g. the presence of oxide or dirt on the surface. Another aspect that may have influenced the detected deviation could be the presence of other particles sintered to the selected couples not on the same focus plane during the measurements. Other particles that participated in the sintering may be absent from the picture because the necks may have broken while handling the start plate. Credibly, the soft grey areas indicated with arrows in Fig. 8d may be the marks of broken necks. Another aspect that should be considered is the rigid motion of the particles during the sintering, which is a challenging modelling aspect to be implemented and adequately experimentally validated [83].

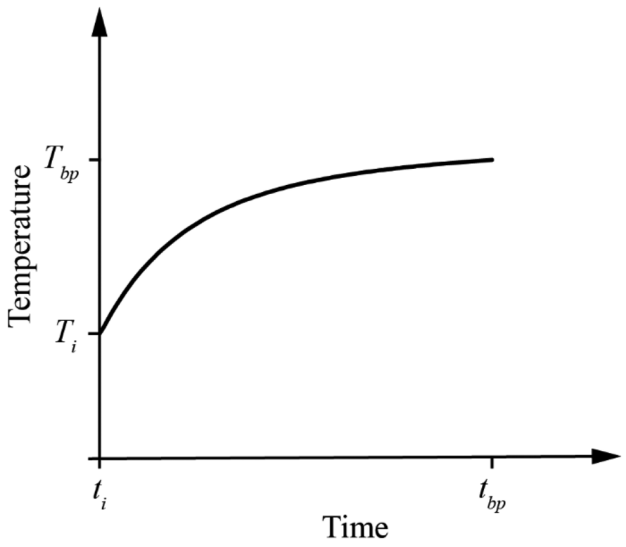


Fig. 7 Temperature evolution during the raking phase

Table 3 Material properties adopted to simulate sintering of Ti6Al4V powder particles

Property	Value	Units	Reference
ϑ_{GB}	10^{-11}	$m^4\ J^{-1}\ s^{-1}$	[42]
γ_{GB}	0.81	$J\ m^{-2}$	[81]
γ_S	2.1	$J\ m^{-2}$	[81]
Q_s	1.19×10^{-19}	J	[42]
$D^0{}_S$	9.33×10^{-8}	$m^2\ s^{-1}$	[42]
Q_v	3.2×10^{-19}	J	[82]
$D^0{}_V$	2.92×10^{-19}	$m^2\ s^{-1}$	[82]
Ω	4.051×10^{-29}	m^3	

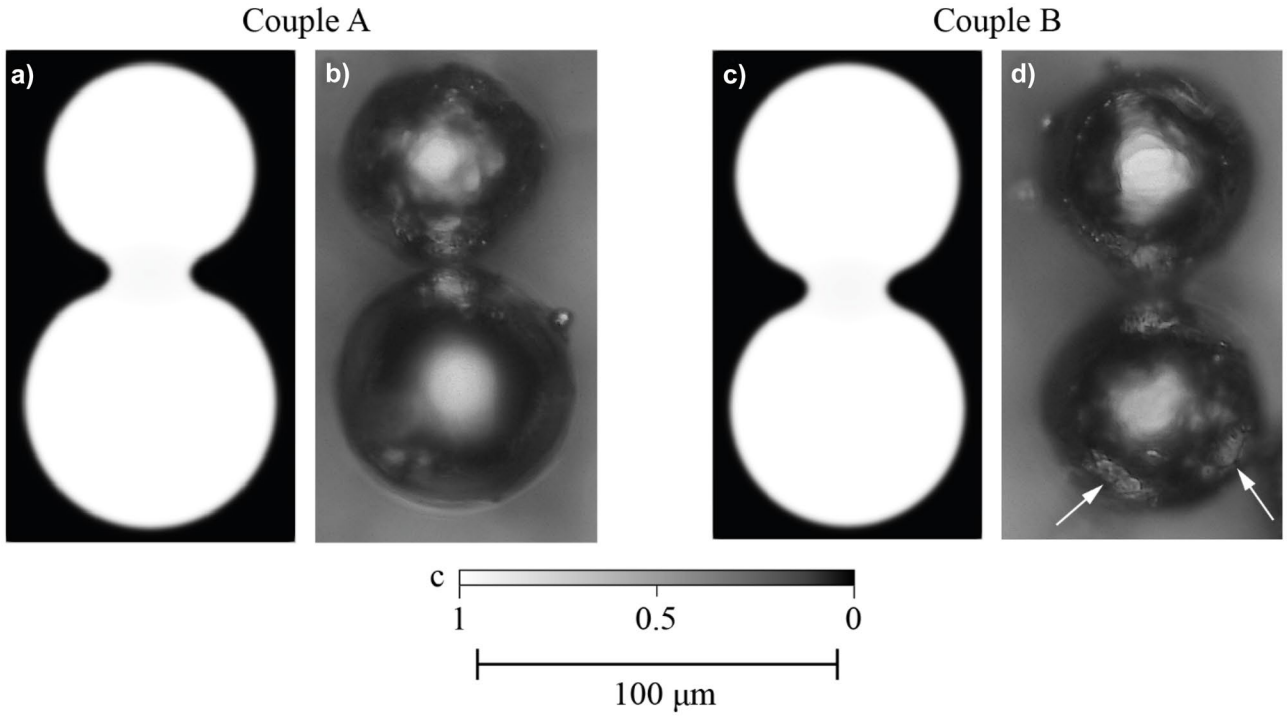


Fig. 8 **a** and **c** Concentration field obtained from the phase-field simulations and **b** and **d** optical microscopy images. White arrows indicate possible marks of broken necks

For completeness, Fig. 9 reports the processing temperature profile with the corresponding simulated neck radius evolution for couples A and B. Owing to the slight differences in the particle diameters, the two curves overlap. As can be observed, the neck growth proceeds rapidly in the first stage of the sintering. It also continues during the cooling phase up to about 800 K. Surprisingly, the neck growth after the preheating (during the cooling) is about 30% higher than the counterparts measured at the end of the preheating (15.26 µm and 15.08 µm for couple A and B, respectively). This neck growth is evident comparing the concentration field reported in Fig. 9a, b. For temperatures below 800 K, the neck growth stops. It is reasonable to assume that this temperature (800 K) could be the sintering initiation temperature for Ti6Al4V powders with the granulometric characteristics considered in the simulation. The differences between the concentration field reported in Fig. 9b, c are negligible. These findings indicate the importance of considering the whole EB-PBF temperature history when analysing the neck growth, affecting the powder thermal and electrical conductivity.

Table 4 Summary of experimental neck diameter measured from optical microscopy images, simulation neck diameter obtained from phase-field simulations and deviation of the simulation neck diameter with respect to experimental mean neck diameter

Couple	Experimental neck diameter [µm]	Numerical neck diameter [µm]	Deviation
A	18.12 ± 6.87	19.70	9%
B	18.91 ± 2.30	19.62	4%

6 Effect of sintering conditions on neck radius and growth

The effect of sintering conditions on neck radius and growth was captured with numerical simulations performed by varying the calculation domain and the thermal load. In particular, the neck radiuses and growths were compared in the case of considering or not delays in the sintering process. Further, the neck radiuses and growths were analysed considering a group of three particles with different dimensions in contact with each other at one single point. Finally, the sintering of two particles was simulated to consider the heat transfer during the phase corresponding to the segment DE (Fig. 2) and, therefore, a total processing time exceeding the construction of the critical substrate [45]. The results of this last simulation were compared with a corresponding simulation performed at a constant temperature all over the process.

In all simulations, the main hypothesis was to capture the sintering behaviour of particles located in a layer sufficiently far from the start plate to avoid any thermal effect. The working temperature (T_w in Fig. 2) was considered equal

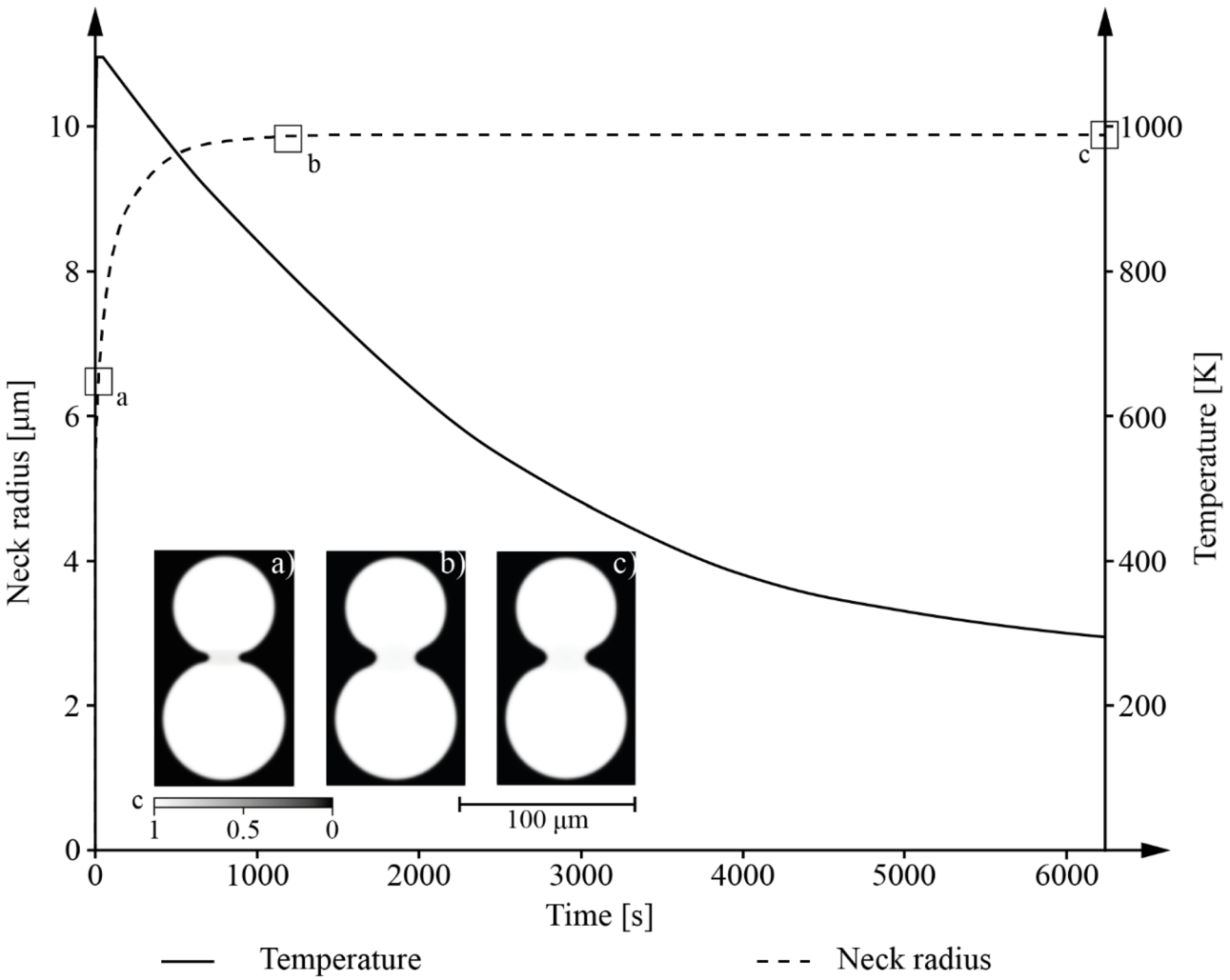


Fig. 9 Neck radius of couple A and B (Fig. 5b)) and temperature evolution during the validation simulation. **a**, **b** and **c** Concentration field from phase-field simulation of couple A (Fig. 8) at different time steps: **a** 60 s; **b** 1200 s; **c** 6240 s

to 973 K [84, 85]. The Ti6Al4V properties adopted for the simulations are reported in Table 1. The additional unvaried parameters valid for all simulations are reported in Table 5. The processing temperature equation for each section of the processing temperature profile (Fig. 2) is reported in Eq. (27), in which the preheating temperature (segment BC in Fig. 2) was increased from T_{bp} to T_p using 25 equally spaced steps.

$$T(t) = \begin{cases} 845 + int\left(\frac{t-4.4}{0.38}\right) \cdot 17.12 & \forall 4.4 \le t \le 13.9 \\ 1273 - 5.82(t - 13.9) & \forall 13.9 < t \le 65.4 \\ 973 & \forall t > 65.4 \end{cases} \quad (27)$$

Table 5 Temperatures and times adopted for the description of the processing temperature for all simulations

Simulation input	Value
T_i	353 K
T_{bp}	845 K
T_p	1273 K [86]
T_w	973 K
T_{bp}	4.4 s
T_p	13.9 s
T_w	65.4 s

6.1 Preheating of two powder particles with the same diameter, applying a delay in sintering initiation

As mentioned in the introduction section, the delay in the sintering initiation may affect the neck radius and growth. Numerically, the sintering was inhibited for a specified time corresponding to the incubation time [68, 69], while the temperature was increased according to Table 3 and Eq. (27).

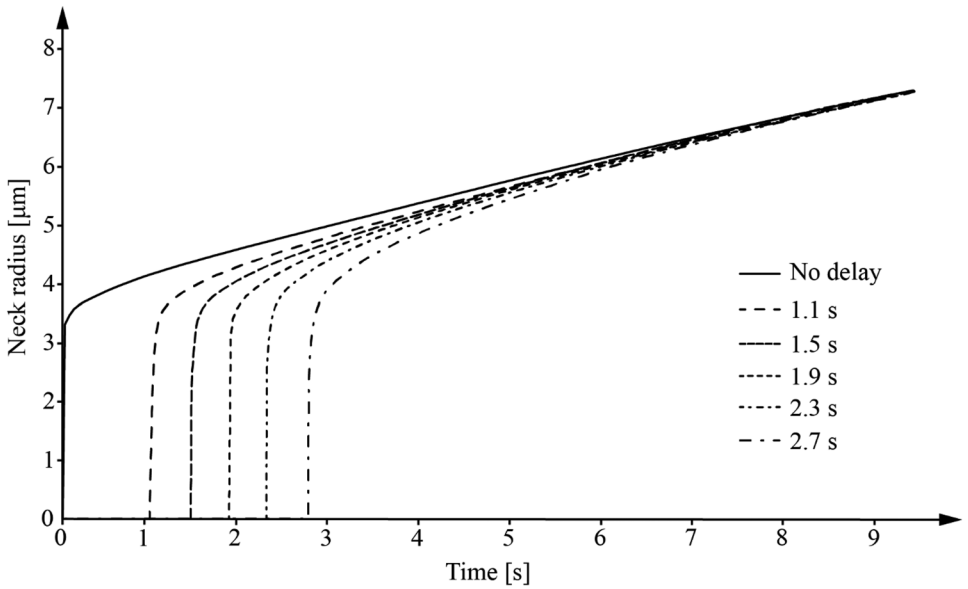


Fig. 10 Neck radius evolution considering and without considering a delay in sintering start

The sintering simulations considered two spherical powder particles with a diameter of 80 μm, a simulation domain of 170 μm × 90 μm and a mesh size of 1 μm. The initial time step was set at 10^{-7} s and adaptively changed, fixing a maximum time step dimension equal to 0.05 s to avoid simulation instabilities. Six sintering simulations were conducted. One neglected the incubation time, while the other five considered different delays in sintering start: 1.1 s; 1.5 s; 1.9 s; 2.3 s and 2.7 s.

Figure 10 and Table 6 compare the neck radius evolution along with the different simulations and report the neck radius growth ratio obtained considering the different simulations with different sintering time delays, respectively. In Table 6, the adhesion stage (up to 0.5 s after the sintering initiation), where the initial neck is formed instantaneously [87], was neglected. Significant differences can be observed in the neck radius evolution. The simulations showed that a sintering delay influences the sintering of powder particles, with a neck radius significantly smaller, at the beginning of preheating. Over the preheating time, the neck radius between the powder particles sintered without the application of sintering delay was always larger than in the other simulation where the delay was considered. However, the dimension of the neck radius is comparable at the end of all the simulations. This phenomenon indicates a significant difference in the neck growth ratios among the simulation conditions (Table 6). Considering the initial time interval (0.5–1.5 s), the simulations in which the sintering delay is considered showed higher neck radius growth ratios (from 0.59 to 0.74 μm/s, Table 6) with respect to the absence of a delay (0.53 μm/s, Table 6). In particular, the longer the delay, the faster the neck radius growth. After 1.5 s from the sintering initiation, the neck radius growth ratio slows down, up to 4.5 s from the sintering start. The neck radius growth ratio is comparable among the simulations starting from this time. In addition, excluding the first time interval, the simulation without delay showed an almost constant neck growth, while if the delay is applied, the neck growth ratio decreases over time. As an example, in the case of a delay of 2.7 s there is a reduction of about 35%.

Since the same temperature profile was adopted, the differences in the growth ratio could be explained by the temperature at which the sintering starts. The higher this

Table 6 Neck radius growth ratio for different delays in sintering start and different time intervals

Time interval after the sintering initiation	No delay [μm/s]	1.1 s delay [μm/s]	1.5 s delay [μm/s]	1.9 s delay [μm/s]	2.3 s delay [μm/s]	2.7 s delay [μm/s]
0.5 s – 1.5 s	0.53	0.59	0.62	0.68	0.71	0.74
1.5 s – 2.5 s	0.41	0.46	0.48	0.51	0.52	0.54
2.5 s – 3.5 s	0.39	0.43	0.44	0.45	0.45	0.46
3.5 s – 4.5 s	0.39	0.41	0.41	0.41	0.41	0.41
4.5 s – 5.5 s	0.38	0.39	0.39	0.37	0.37	0.37
5.5 s – 6.5 s	0.37	0.37	0.36	0.35	0.35	0.35

Table 7 The diameter ratio of the particles in the simulation. For each couple, d is the diameter of the smaller particle, while D is the diameter of the larger particle. The diameter of particle (1) is 105 µm, the diameter of particle (2) is 80 µm, and the diameter of particle (3) is 45 µm

Contact point	Ratio between the diameters (d/D)
(1)–(2)	0.76
(2)–(3)	0.56
(3)–(1)	0.43

temperature, the higher the neck growth ratio will be, which agrees with Koparde and Cummings [88]. From a process point of view, the delay of sintering may be caused by several factors, such as the presence of dirt or oxide on the surface. However, the numerical investigation revealed that a sintering initiation delay does not affect the final neck dimension and, therefore, the subsequent step of the process, but only the neck growth ratio. Therefore, it is presumable that the energy applied at the beginning of the preheating step of the EB-PBF process is spent only to increase the temperature and, for example, dissolve the oxide layer [68, 69]. This delay in the sintering start may also explain the higher risk of smoke during the first few seconds of the preheating step [46].

6.2 Preheating of three powder particles with different diameters

To account for the presence of multiple particles, the sintering of three particles with a diameter equal to (1) 105 µm, (2) 80 µm and (3) 45 µm, respectively, was simulated. The diameters were selected for having a decreasing diameter ratio (Table 7). The particles are in contact with each other at a single point.

A simulation domain of 170 µm × 175 µm and a mesh size of 1 µm were considered. The initial time step was set to 10^{-3} s and was automatically adapted during the simulation. The maximum dimension of the time step was limited to 0.05 s to avoid simulation instabilities.

Figure 11 compares the neck growth rate between particles (1) and (2), (2) and (3), and (3) and (1). The diameter of the particles participating in the sintering strongly affected the first few seconds of the process. While the neck growth rates associated with particle (3) when touching particles (1) and (2) were comparable (around 0.29 µm/s), it was much higher at the contact point between the biggest particles, (1) and (2), and around 0.33 µm/s. At the end of the simulation,

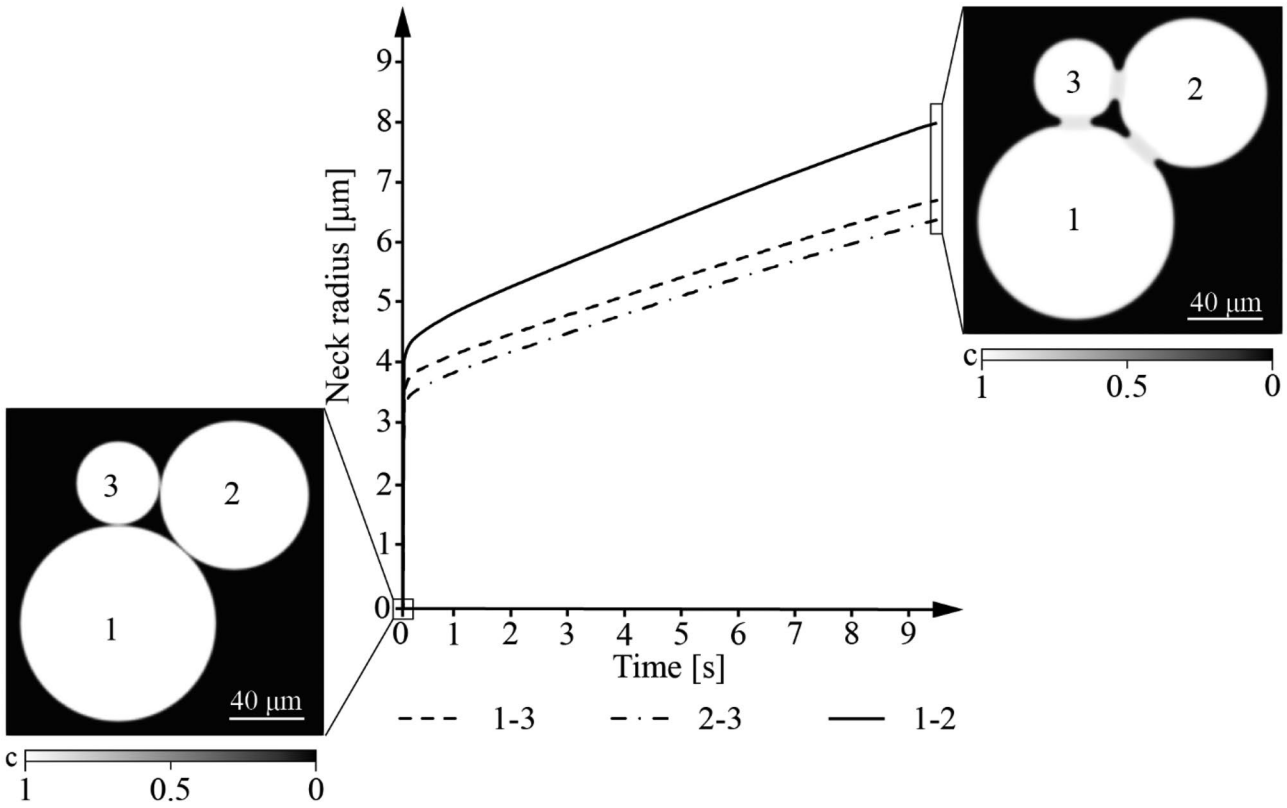


Fig. 11 Necks evolution for the three particles system. The concentration field at the beginning of the simulation and at the end of the simulation is also reported

particles with a larger diameter ratio (Table 7) showed a larger neck. In particular, the measured neck radii were 7.97 µm, 6.37 µm and 6.7 µm between the particles 1–2, 2–3, and 3–1, respectively. However, the previous simulation carried out with two equal particles (ratio between the particles equal to 1), without considering a delay in sintering start, showed a slightly lower value (7.34 µm). This difference can be explained by the influence of the diameters and the ratio between the diameter of the particles on the neck radius. These findings agree with the experimental results reported in Ting and Lin [89] and Gusarov et al. [90]. As indicated by Kandis and Bergman [93], the effect, which may not be linear [89], of the mutual characteristics of the adjacent particles on the sintering/neck radius may become relevant when analysing the effective powder thermal conductivity.

6.3 Sintering two powder particles with the same diameter during the whole EB-PBF process

Sintering of two powder particles with the same diameter (80 µm) has been considered to capture the effect of a longer process time scale on neck growth. The selected time was 3.87 h, corresponding to 13,920 s and a building height of

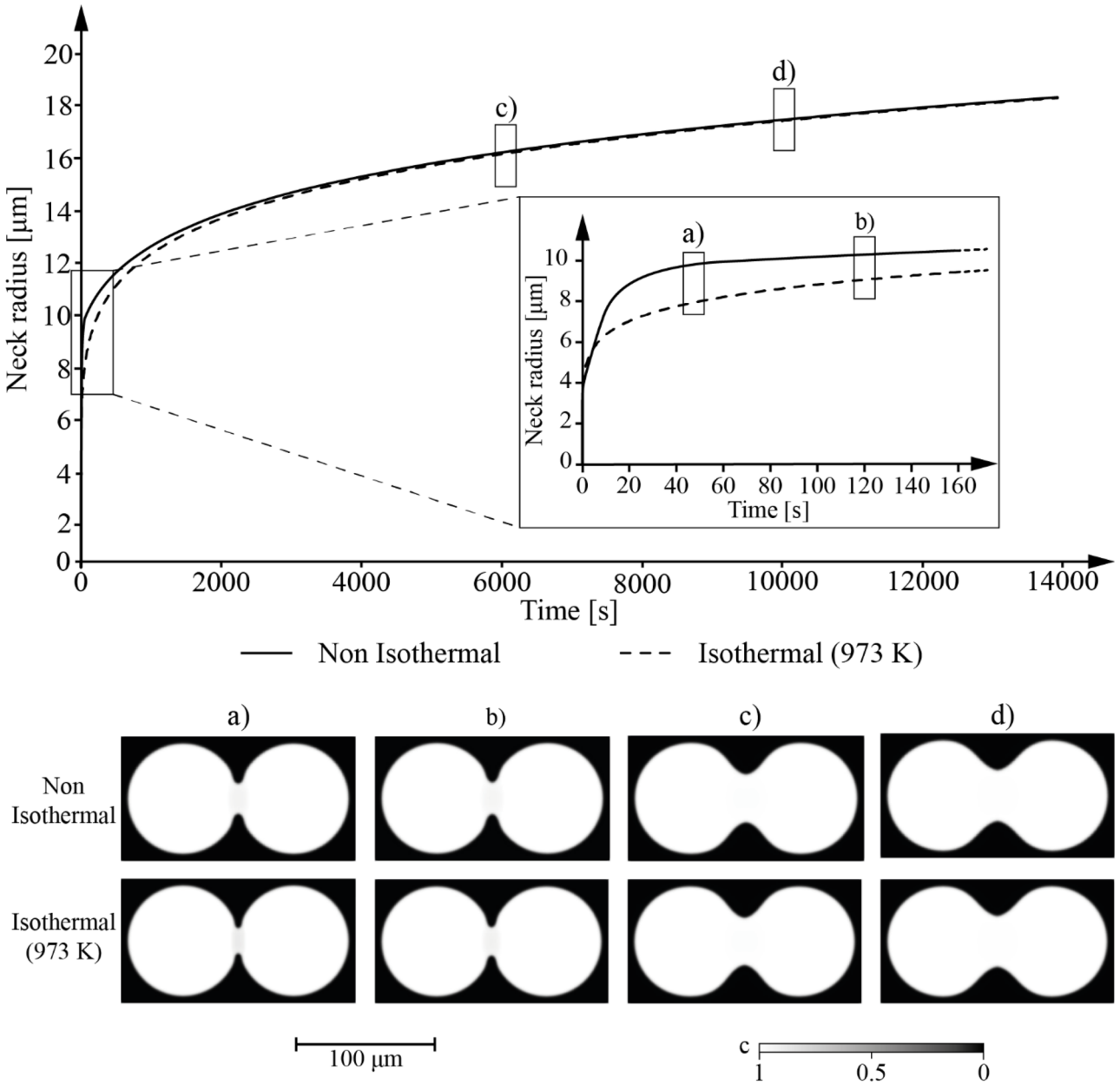


Fig. 12 Neck evolution for constant and variable temperature simulations. The concentration field for the isothermal and non-isothermal simulation is reported at different simulation time steps: **a** 40 s; **b** 120 s; **c** 6000 s; **d** 10,000 s

around 12 mm. This building height has been selected to simulate the sintering behaviour of particles positioned in a layer out of the critical substrate equal to 10 mm [45]. A simulation domain equal to 170 μm × 90 μm and a mesh size of 1 μm were adopted. The time step was adapted according to the time scale associated with each process phase. The temperature was increased according to Table 5 and Eq. (27). For comparison purposes, the same simulation was performed at a constant temperature equal to T_w (Table 5) over the entire simulation time.

Figure 12 compares the obtained numerical results. As can be observed, the neck growth rates over the whole process were significantly different. The neck radius obtained under non-isothermal conditions was always larger than the corresponding one at a constant temperature. The largest deviations can be detected up to almost 4000 s (about 1 h, build height about 3 mm), with the maximum at the beginning of the process, when the formation of the neck plays the central role in ensuring proper thermal and electrical conductivities and supporting the subsequent layers. This difference is highlighted in the magnification of Fig. 12. After 40 s of simulation, the neck radius obtained under non-isothermal conditions is approximately 2 μm larger than that at a constant temperature. Differences between the two simulation results can also be observed from a geometrical point of view. As an example, Fig. 12a–d compares the concentration field for the isothermal and non-isothermal simulations at different times. At 40 s (Fig. 12a) and 120 s (Fig. 12b), the dihedral angle in the case of non-isothermal simulation is larger than the counterpart obtained under isothermal conditions. The differences in the dihedral angle reduce in the later stages of the simulation (e.g. Fig. 12c at 6000 s and Fig. 12d at 10000 s). The differences detected in the neck radius, the neck growth and the dihedral angle will affect the thermophysical properties of the powder bed and, therefore, the overall process. For example, at a selected time, e.g. 457 s in Fig. 12, the neck radius between the particles is about 4.8% larger in the case of non-isothermal conditions. According to Al-Bermani et al. [84], a rough calculation of the thermal conductivity at non-isothermal conditions is about 5.1% higher than the corresponding at iso-thermal conditions.

The hypothesis of sintering under isothermal conditions, such as reported in [42], is more representative considering the sintering behaviour after a couple of hours from the sintering start. However, this time could be longer in the case the heating supplied during the processing of the subsequent layers (contributions (3) and (4)) would have been considered. At the end of the simulation time, under the analysed conditions, the neck radiuses were comparable (for non-isothermal conditions equal to 18.35 μm and counterparts sintered at a constant temperature equal to 18.32 μm).

7 Conclusions

This paper developed new modelling for the thermal load for simulating the non-isothermal sintering during an EB-PBF process. Different thermal contributions have been considered to emulate the actual heat transfer during an EB-PBF and implemented in a phase-field model. The model validation showed a good agreement between the experimental and the numerical results, with a maximum deviation of 9%. The findings of this work can be resumed as follows:

- During the cooling phase, the neck growth continues up to around 800 K. This highlights that the neck radius, which influences the powder bed thermal and electrical conductivities, varies significantly during the process.
- Delays in the sintering initiation caused a larger neck growth ratio, which allowed obtaining, at the end of the preheating, a comparable neck radius to the corresponding simulation without a sintering delay.
- The particle diameters and their ratio influenced the sintering degree of adjacent particles significantly.
- The non-isothermal condition during an EB-PBF influenced the neck growth greatly. The hypothesis of sintering under isothermal conditions is more representative considering the sintering behaviour after a couple of hours from the sintering initiation. However, considering that the sintering already starts at the preheating step, where the neck formation is more critical for the process, the hypothesis of sintering under isothermal conditions is incorrect at a smaller time scale (up to 1 h from the sintering initiation under the investigated conditions).
- The model could be valuable to evaluate the neck radius at any time during the process and, therefore, the powder bed properties, such as thermal conductivity, without performing any challenging sintering experiments or using an extensive and expensive measuring system, such as CT-Scan analysis [50].

Future works are needed to validate the model response under different processed materials and more detailed processing conditions, which consider the contribution due to the heating supplied when processing the subsequent layers (contributions (3) and (4)). With this regard, additional research efforts will be required to characterize the neck shape during the EB-PBF since, up today, measurements have been performed only with cold sintered powder [50], and thermal conductivities have been calculated without considering the vacuum conditions [49, 50, 91].

The proposed model for the temperature history can also be easily extended to simulate other AM powder bed fusion processes, such as selective laser sintering or traditional sintering of ceramic materials, where the effect of non-isothermal conditions on a short or long time scale may be relevant [92, 93].

Author contribution Giovanni Rizza and Manuela Galati contributed to the study conception and design. Material preparation, data collection and analysis were performed by Giovanni Rizza and Manuela Galati. The first draft of the manuscript was written by Giovanni Rizza and all authors commented on previous versions of the manuscript. Luca Iuliano made available the experimental and computational resources. All authors read and approved the final manuscript.

Funding Open access funding provided by Politecnico di Torino within the CRUI-CARE Agreement.

Declarations

Competing interests The authors declare no competing interests.

Open Access This article is licensed under a Creative Commons Attribution 4.0 International License, which permits use, sharing, adaptation, distribution and reproduction in any medium or format, as long as you give appropriate credit to the original author(s) and the source, provide a link to the Creative Commons licence, and indicate if changes were made. The images or other third party material in this article are included in the article's Creative Commons licence, unless indicated otherwise in a credit line to the material. If material is not included in the article's Creative Commons licence and your intended use is not permitted by statutory regulation or exceeds the permitted use, you will need to obtain permission directly from the copyright holder. To view a copy of this licence, visit http://creativecommons.org/licenses/by/4.0/.

References

1. German R (2014) Sintering: From Empirical Observations to Scientific Principles. 1-536. Elsevier Ltd. https://doi.org/10.1016/C2012-0-00717-X
2. Kang SJL (2005) Sintering: Densification, grain growth and microstructure. 1–265. Elsevier Ltd. https://doi.org/10.1016/B978-0-7506-6385-4.X5000-6
3. Dzepina B, Balint D, Dini D (2019) A phase field model of pressure-assisted sintering. J Eur Ceram Soc 39:173–182. https://doi.org/10.1016/j.jeurceramsoc.2018.09.014
4. Ashby MF (1974) A first report on sintering diagrams. Acta Metall 22:275–289. https://doi.org/10.1016/0001-6160(74)90167-9
5. Torres Y, Pavón JJ, Nieto I, Rodríguez JA (2011) Conventional powder metallurgy process and characterization of porous titanium for biomedical applications. Metall Mater Trans B 42:891–900 https://doi.org/10.1007/s11663-011-9521-6
6. Del Guercio G, Galati M, Saboori A et al (2020) Microstructure and mechanical performance of Ti–6Al–4V lattice structures manufactured via electron beam melting (ebm): a review. Acta Metall Sin (Eng Lett) 33:183–203
7. Lunetto V, Galati M, Settineri L, Iuliano L (2020) Unit process energy consumption analysis and models for Electron Beam Melting (EBM): effects of process and part designs. Addit Manuf 33:101115. https://doi.org/10.1016/j.addma.2020.101115
8. Galati M, Iuliano L (2018) A literature review of powder-based electron beam melting focusing on numerical simulations. Addit Manuf 19:1–20. https://doi.org/10.1016/j.addma.2017.11.001
9. Cheng B, Price S, Lydon J et al (2014) On process temperature in powder-bed electron beam additive manufacturing: model development and validation. J Manuf Sci Eng Trans ASME 136:1–12. https://doi.org/10.1115/1.4028484
10. Larsson M, Snis A (2008) Method and device for producing three-dimensional objects. Patent number: EP2049289B1 objects. Current assignee: Arcam AB. Publication 30-04-2014
11. Zhang J, Zhang Y, Lee WH et al (2018) A multi-scale multi-physics modeling framework of laser powder bed fusion additive manufacturing process. Met Powder Rep 73:151–157. https://doi.org/10.1016/j.mprp.2018.01.003
12. Sahoo S (2020) Consolidation behavior of metal powders in laser additive manufacturing. Met Powder Rep. https://doi.org/10.1016/J.MPRP.2020.06.060
13. Raychaudhuri S (2008) Introduction to monte carlo simulation. Proc Winter Simul Conf 91–100
14. Tikare V, Braginsky M, Olevsky EA (2003) Numerical simulation of solid-state sintering: I, sintering of three particles. J Am Ceram Soc 86:49–53. https://doi.org/10.1111/j.1151-2916.2003.tb03276.x
15. Ye B, Matsen MR, Dunand DC (2012) Finite-element modeling of titanium powder densification. Metall Mater Trans A Phys Metall Mater Sci 43:381–390. https://doi.org/10.1007/s11661-011-0839-0
16. Biswas S, Schwen D, Singh J, Tomar V (2016) A study of the evolution of microstructure and consolidation kinetics during sintering using a phase field modeling based approach. Extrem Mech Lett 7:78–89. https://doi.org/10.1016/j.eml.2016.02.017
17. Wang YU (2006) Computer modeling and simulation of solid-state sintering: a phase field approach. Acta Mater 54:953–961. https://doi.org/10.1016/j.actamat.2005.10.032
18. Pan J (2003) Modelling sintering at different length scales. Int Mater Rev 48:69–85. https://doi.org/10.1179/095066002225010209
19. Hu SY, Henager CH (2010) Phase-field simulation of void migration in a temperature gradient. Acta Mater 58:3230–3237. https://doi.org/10.1016/j.actamat.2010.01.043
20. Loginova I, Amberg G, Ågren J (2001) Phase-field simulations of non-isothermal binary alloy solidification. Acta Mater 49:573–581. https://doi.org/10.1016/S1359-6454(00)00360-8
21. Wang X (2018) Chou K (2018) Microstructure simulations of Inconel 718 during selective laser melting using a phase field model. Int J Adv Manuf Technol 1009(100):2147–2162. https://doi.org/10.1007/S00170-018-2814-Z
22. Jin YM, Artemev A, Khachaturyan AG (2001) Three-dimensional phase field model of low-symmetry martensitic transformation in polycrystal: Simulation of ζ′2 martensite in AuCd alloys. Acta Mater 49:2309–2320. https://doi.org/10.1016/S1359-6454(01)00108-2
23. Kazaryan A, Wang Y, Dregia S (2000) Generalized phase-field model for computer simulation of grain growth in anisotropic systems. Phys Rev B - Condens Matter Mater Phys 61:14275–14278. https://doi.org/10.1103/PhysRevB.61.14275
24. Uehara T, Tsujino T, Ohno N (2007) Elasto-plastic simulation of stress evolution during grain growth using a phase field model. J Cryst Growth 300:530–537. https://doi.org/10.1016/j.jcrysgro.2006.12.045
25. Hu SY, Chen LQ (2001) Solute segregation and coherent nucleation and growth near a dislocation - a phase-field model integrating defect and phase microstructures. Acta Mater 49:463–472. https://doi.org/10.1016/S1359-6454(00)00331-1
26. Hu SY, Baskes MI, Stan M (2007) Phase-field modeling of microvoid evolution under elastic-plastic deformation. Appl Phys Lett 90:081921. https://doi.org/10.1063/1.2709908
27. Aranson IS, Kalatsky VA, Vinokur VM (2000) Continuum field description of crack propagation. Phys Rev Lett 85:118–121. https://doi.org/10.1103/PhysRevLett.85.118
28. Karma A, Kessler DA, Levine H (2001) Phase-field model of mode III dynamic fracture. Phys Rev Lett 87:45501-1-45501–4. https://doi.org/10.1103/PhysRevLett.87.045501
29. Esmaeilzadeh P, Behnagh RA, Pour MAM et al (2020) Phase-field modeling of fracture and crack growth in friction stir processed pure copper. Int J Adv Manuf Technol 109:2377–2392. https://doi.org/10.1007/S00170-020-05488-3/FIGURES/17

30. Chen LQ (2002) Phase-field models for microstructure evolution. Annu Rev Mater Sci 32:113–140
31. Bailey NS, Shin YC (2022) Multi-track, multi-layer dendrite growth and solid phase transformation analysis during additive manufacturing of H13 tool steel using a combined hybrid cellular automata/phase field, solid-state phase prediction models. Int J Adv Manuf Technol 120:2089–2108. https://doi.org/10.1007/S00170-022-08901-1/FIGURES/21
32. Moelans N, Blanpain B, Wollants P (2008) An introduction to phase-field modeling of microstructure evolution. Calphad Comput Coupling Phase Diagrams Thermochem 32:268–294. https://doi.org/10.1016/j.calphad.2007.11.003
33. Deng J (2012) A phase field model of sintering with direction-dependent diffusion. https://doi.org/10.2320/matertrans.M2011317
34. Biswas S, Schwen D, Tomar V (2018) Implementation of a phase field model for simulating evolution of two powder particles representing microstructural changes during sintering. J Mater Sci 53:5799–5825. https://doi.org/10.1007/s10853-017-1846-3
35. Wang H, Biswas S, Han Y, Tomar V (2018) A phase field modeling based study of microstructure evolution and its influence on thermal conductivity in polycrystalline tungsten under irradiation. Comput Mater Sci 150:169–179. https://doi.org/10.1016/j.commatsci.2018.03.070
36. Biswas S, Schwen D, Wang H et al (2018) Phase field modeling of sintering: Role of grain orientation and anisotropic properties. Comput Mater Sci 148:307–319. https://doi.org/10.1016/j.commatsci.2018.02.057
37. Zhang X, Liao Y (2018) A phase-field model for solid-state selective laser sintering of metallic materials. Powder Technol 339:677–685. https://doi.org/10.1016/j.powtec.2018.08.025
38. Yang Y, Ragnvaldsen O, Bai Y et al (2019) 3D non-isothermal phase-field simulation of microstructure evolution during selective laser sintering. npj Comput Mater 51(5):1–12. https://doi.org/10.1038/s41524-019-0219-7
39. Wang X, Liu Y, Li L et al (2021) Multi-scale phase-field modeling of layer-by-layer powder compact densification during solid-state direct metal laser sintering. Mater Des 203:109615. https://doi.org/10.1016/j.matdes.2021.109615
40. Gong X, Chou K (2015) Phase-field modeling of microstructure evolution in electron beam additive manufacturing. JOM 675(67):1176–1182. https://doi.org/10.1007/S11837-015-1352-5
41. Sahoo S, Chou K (2016) Phase-field simulation of microstructure evolution of Ti–6Al–4V in electron beam additive manufacturing process. Addit Manuf 9:14–24. https://doi.org/10.1016/J.ADDMA.2015.12.005
42. Yan W, Ma W, Shen Y (2020) Powder sintering mechanisms during the pre-heating procedure of electron beam additive manufacturing. Mater Today Commun 25:101579. https://doi.org/10.1016/j.mtcomm.2020.101579
43. Landau E, Tiferet E, Ganor YI et al (2020) Thermal characterization of the build chamber in electron beam melting. Addit Manuf 36:101535. https://doi.org/10.1016/J.ADDMA.2020.101535
44. Shen N, Chou K (2013) Thermal modeling of electron beam additive manufacturing process: powder sintering effects. ASME Int Manuf Sci Eng Conf Collocated North Am Manuf Res Conf Particip Int Conf MSEC 2012:287–295. https://doi.org/10.1115/MSEC2012-7253
45. Shen N, Chou K (2012) Numerical thermal analysis in electron beam additive manufacturing with preheating effects. Ann Int Solid Freeform Fabr Sympn Addit Manuf Conf SFF 774–784
46. Cordero ZC, Meyer HM, Nandwana P, Dehoff RR (2017) Powder bed charging during electron-beam additive manufacturing. Acta Mater 124:437–445. https://doi.org/10.1016/j.actamat.2016.11.012
47. Sigl M, Lutzmann S, Zäh MF (2006) Transient physical effects in electron beam sintering. Int Solid Freeform Fabr Symp
48. Qi HB, Yan YN, Lin F et al (2006) Direct metal part forming of 316L stainless steel powder by electron beam selective melting. Proc Inst Mech Eng Part B J Eng Manuf 220:1845–1853. https://doi.org/10.1243/09544054JEM438
49. Smith CJ, Tammas-Williams S, Hernandez-Nava E, Todd I (2017) Tailoring the thermal conductivity of the powder bed in Electron Beam Melting (EBM) Additive Manufacturing. Sci Rep 7:1–8. https://doi.org/10.1038/s41598-017-11243-8
50. Leung CLA, Tosi R, Muzangaza E et al (2019) Effect of preheating on the thermal, microstructural and mechanical properties of selective electron beam melted Ti-6Al-4V components. Mater Des 174:107792. https://doi.org/10.1016/j.matdes.2019.107792
51. Cheng B, Chou K (2015) Geometric consideration of support structures in part overhang fabrications by electron beam additive manufacturing. Comput Des 69:102–111. https://doi.org/10.1016/J.CAD.2015.06.007
52. Galati M, Saboori A, Biamino S et al (2020) Ti-6Al-4V lattice structures produced by EBM: Heat treatment and mechanical properties. In Procedia CIRP. Elsevier B.V., pp 411–416
53. Galati M, Rizza G, Defanti S, Denti L (2021) Surface roughness prediction model for Electron Beam Melting (EBM) processing Ti6Al4V. Precis Eng 69:19–28. https://doi.org/10.1016/j.precisioneng.2021.01.002
54. Körner C (2016) Additive manufacturing of metallic components by selective electron beam melting - A review. Int Mater Rev 61:361–377
55. Algardh JK, Horn T, West H et al (2016) Thickness dependency of mechanical properties for thin-walled titanium parts manufactured by Electron Beam Melting (EBM)®. Addit Manuf 12:45–50. https://doi.org/10.1016/j.addma.2016.06.009
56. Kahnert M, Lutzmann S, Zaeh MF (2007) Layer formations in electron beam sintering. In: 18th Solid Freeform Fabrication Symposium, SFF 2007. pp 88–99
57. Honda K (2017) Machine and method for additive manufacturing. Patent Number: US9452489B2. Current Assignee: Jeol Ltd. Publication: 27-07-2016
58. Hrabe N, Gnäupel-Herold T, Quinn T (2017) Fatigue properties of a titanium alloy (Ti–6Al–4V) fabricated via electron beam melting (EBM): Effects of internal defects and residual stress. Int J Fatigue 94:202–210. https://doi.org/10.1016/j.ijfatigue.2016.04.022
59. Galati M, Snis A, Iuliano L (2019) Powder bed properties modelling and 3D thermo-mechanical simulation of the additive manufacturing Electron Beam Melting process. Addit Manuf 30:100897. https://doi.org/10.1016/J.ADDMA.2019.100897
60. Baudana G, Biamino S, Klöden B et al (2016) Electron beam melting of Ti-48Al-2Nb-0.7Cr-0.3Si: feasibility investigation. Intermetallics 73:43–49. https://doi.org/10.1016/j.intermet.2016.03.001
61. Goel S, Mehtani H, Yao SW et al (2020) As-built and post-treated microstructures of an electron beam melting (EBM) produced nickel-based superalloy. Metall Mater Trans A Phys Metall Mater Sci 51:6546–6559. https://doi.org/10.1007/s11661-020-06037-z
62. Tang HP, Qian M, Liu N et al (2015) Effect of powder reuse times on additive manufacturing of Ti-6Al-4V by selective electron beam melting. JOM 67:555–563. https://doi.org/10.1007/s11837-015-1300-4
63. Bonifacio CS, Rufner JF, Holland TB, Van Benthem K (2012) In situ transmission electron microscopy study of dielectric breakdown of surface oxides during electric field-assisted sintering of nickel nanoparticles. Appl Phys Lett 101:93107. https://doi.org/10.1063/1.4749284
64. Franchitti S, Borrelli R, Pirozzi C et al (2018) Investigation on electron beam melting: dimensional accuracy and process repeatability. Vacuum 157:340–348. https://doi.org/10.1016/j.vacuum.2018.09.007
65. Karlsson J, Snis A, Engqvist H, Lausmaa J (2013) Characterization and comparison of materials produced by Electron Beam Melting (EBM) of two different Ti–6Al–4V powder fractions. J

Mater Process Technol 213:2109–2118. https://doi.org/10.1016/J.JMATPROTEC.2013.06.010
66. Gruber H, Henriksson M, Hryha E (2019) Nyborg L (2019) Effect of powder recycling in electron beam melting on the surface chemistry of alloy 718 powder. Metall Mater Trans A 509(50):4410–4422. https://doi.org/10.1007/S11661-019-05333-7
67. Takahashi Y, Nakamura T, Nishiguchi K (1992) Dissolution process of surface oxide film during diffusion bonding of metals. J Mater Sci 27:485–498. https://doi.org/10.1007/BF00543942
68. Munir ZA (1981) Surface oxides and sintering of metals. Powder Metall 24:177–180. https://doi.org/10.1179/pom.1981.24.4.177
69. Munir ZA (1979) Analytical treatment of the role of surface oxide layers in the sintering of metals. J Mater Sci 14:2733–2740. https://doi.org/10.1007/BF00610647
70. Watanabe T, Horikoshi Y (1976) The sintering phenomenon of titanium powders: a discussion. Int J Powder Metall Powder Technol 12:209–214
71. Cao Y, Delin M, Kullenberg F, Nyborg L (2020) Surface modification of Ti-6Al-4V powder during recycling in EBM process. In Surface and Interface Analysis. John Wiley and Sons Ltd, pp 1066–1070
72. Shen N, Chou YK (2012) Numerical thermal analysis in electron beam additive manufacturing with preheating effects. In Proceedings of the 23rd Solid Freeform Fabrication Symposium, Austin, TX. pp 774–784
73. Chockalingam K, Kouznetsova VG, van der Sluis O, Geers MGD (2016) 2D Phase field modeling of sintering of silver nanoparticles. Comput Methods Appl Mech Eng 312:492–508. https://doi.org/10.1016/j.cma.2016.07.002
74. Permann CJ, Gaston DR, Andrš D et al (2020) MOOSE: enabling massively parallel multiphysics simulation. SoftwareX 11:100430. https://doi.org/10.1016/j.softx.2020.100430
75. Chen CC, Tsai YL, Lan CW (2009) Adaptive phase field simulation of dendritic crystal growth in a forced flow: 2D vs 3D morphologies. Int J Heat Mass Transf 52:1158–1166. https://doi.org/10.1016/J.IJHEATMASSTRANSFER.2008.09.014
76. Galati M (2021) Electron beam melting process. In Additive Manufacturing. Elsevier, pp 277–301
77. Ivannikov V, Thomsen F, Ebel T, Willumeit-Römer R (2021) Capturing shrinkage and neck growth with phase field simulations of the solid state sintering. Model Simul Mater Sci Eng 29:075008. https://doi.org/10.1088/1361-651X/AC1F87
78. Galati M, Iuliano L, Salmi A, Atzeni E (2017) Modelling energy source and powder properties for the development of a thermal FE model of the EBM additive manufacturing process. Addit Manuf 14:49–59. https://doi.org/10.1016/j.addma.2017.01.001
79. Galati M, Snis A, Iuliano L (2019) Experimental validation of a numerical thermal model of the EBM process for Ti6Al4V. Comput Math Appl 78:2417–2427. https://doi.org/10.1016/j.camwa.2018.07.020
80. Chandrasekar S, Coble JB, Yoder S et al (2020) Investigating the effect of metal powder recycling in Electron beam Powder Bed Fusion using process log data. Addit Manuf 32:100994. https://doi.org/10.1016/j.addma.2019.100994
81. Roth TA, Suppayak P (1978) The surface and grain boundary free energies of pure titanium and the titanium alloy Ti6Al4V. Mater Sci Eng 35:187–196. https://doi.org/10.1016/0025-5416(78)90120-9
82. Nemat-Nasser S, Guo WG, Cheng JY (1999) Mechanical properties and deformation mechanisms of a commercially pure titanium. Acta Mater 47:3705–3720. https://doi.org/10.1016/S1359-6454(99)00203-7
83. Shi R, Wood M, Heo TW et al (2021) Towards understanding particle rigid-body motion during solid-state sintering. J Eur Ceram Soc 41:211–231. https://doi.org/10.1016/j.jeurceramsoc.2021.09.039
84. Al-Bermani SS, Blackmore ML, Zhang W (2010) Todd I (2010) The origin of microstructural diversity, texture, and mechanical properties in electron beam melted Ti-6Al-4V. Metall Mater Trans A 4113(41):3422–3434. https://doi.org/10.1007/S11661-010-0397-X
85. Jamshidinia M, Kovacevic R (2015) The influence of heat accumulation on the surface roughness in powder-bed additive manufacturing. Surf Topogr Metrol Prop 3:014003. https://doi.org/10.1088/2051-672X/3/1/014003
86. Galati M, Snis A, Iuliano L (2018) Experimental validation of a numerical thermal model of the EBM process for Ti6Al4V. Comput Math Appl
87. Swinkels FB, Ashby MF (1981) A second report on sintering diagrams. Acta Metall 29:259–281. https://doi.org/10.1016/0001-6160(81)90154-1
88. Koparde VN, Cummings PT (2005) Molecular dynamics simulation of titanium dioxide nanoparticle sintering. J Phys Chem B 109:24280–24287. https://doi.org/10.1021/jp054667p
89. Ting J-M, Lin RY (1994) Effect of particle-size distribution on sintering - Part I Modelling. J Mater Sci 29:1867–1872. https://doi.org/10.1007/BF00351306
90. Gusarov AV, Laoui T, Froyen L, Titov VI (2003) Contact thermal conductivity of a powder bed in selective laser sintering. Int J Heat Mass Transf 46:1103–1109. https://doi.org/10.1016/S0017-9310(02)00370-8
91. Gong X, Chou K (2013) Characterization of Sintered Ti-6Al-4V Powders in Electron Beam Additive Manufacturing. ASME 2013 Int Manuf Sci Eng Conf Collocated with 41st North Am Manuf Res Conf MSEC 2013. https://doi.org/10.1115/MSEC2013-1131
92. Han J, Senos AMR, Mantas PQ (1999) Nonisothermal sintering of Mn doped ZnO. J Eur Ceram Soc 19:1003–1006. https://doi.org/10.1016/S0955-2219(98)00362-8
93. Kandis M, Bergman TL (1997) Observation, prediction, and correlation of geometric shape evolution induced by non-isothermal sintering of polymer powder. J Heat Transfer 119:824–831. https://doi.org/10.1115/1.2824189

Publisher's Note Springer Nature remains neutral with regard to jurisdictional claims in published maps and institutional affiliations.